IMPROVEMENT OF ACCURACY IN DEFORMABLE REGISTRATION IN RADIATION THERAPY

Xiaojing Ye and Yunmei Chen

Department of Mathematics, University of Florida, 358 Little Hall, Gainesville, FL 32611-8105

ABSTRACT

In this paper, we propose a segmentation assisted registration model. It partitions the domain of images into several regions such that the residue image in each region is identically distributed with zero mean and variance to be optimized. In this model, we minimize an energy that combines negative log-likelihood of the residue in each region, smoothness of the deformation field and length of the partition curve. It can be viewed as a generalization of the sum of squared difference model and global Gaussian model where the variance is a constant in the entire domain. By taking different variances in different regions, the registration becomes more efficient and accurate, which are demonstrated by the experiments on synthetic and clinical data.

Index Terms— deformation, registration, Gaussian noise, finite difference method, partial differential equations.

1. INTRODUCTION

The importance of registration cannot be more emphasized in the study of modern computer vision and image processing. The main purpose of image registration is to align two or more images by mapping points in one image to corresponding points in another. The mapping, or transformation, can be rigid or non-rigid. Rigid registration has restrictions that the transformation can only be scaling, rotation, translation or their compositions, and is therefore not adequate in modern radiotherapy applications. On the other hand, non-rigid, or so-called deformable registration, accounts for internal organ deformation, and allows more precise tumor targeting and preservation of normal tissues, so it becomes the key technique in most practical applications such as radiation therapy[1].

Deformable image registration has been extensively studied in the literature[2, 3, 4, 5]. Among those widely used deformable registration models, variational method is one of the most important and effective approaches. For simplicity, let Ω be a bounded open set in $\mathbb{R}^2$. The template image T and study image S are given as intensity functions defined on Ω. Along with dissimilarity term, the method of Lagrange multiplier turns regularity constraint into a penalty term in energy functional. Then variational method presents deformable registration as a minimization problem of deformation $\vec{u} = \arg\min_{\vec{u}\in\mathscr{A}} E[\vec{u}]$ where the energy functional $E[\vec{u}]$ is defined by

$$E[\vec{u}] = \text{regularity}(\vec{u}) + \text{dissimilarity}(T(\vec{x}-\vec{u}), S(\vec{x})), \quad (1)$$

and $\mathscr{A}$ is the admissible set of deformations $\vec{u} : \Omega \to \Omega$. One measure of the difference between $T(\vec{x}-\vec{u})$ and $S(\vec{x})$ in (1) is the sum of squared difference (SSD), or L^2 norm in continues form[2, 6]. If the regularity of $\vec{u}$ is proposed as coordinate-wise L^2 norm of $\nabla\vec{u}$, then the energy functional can be explicitly written as

$$E[\vec{u}] = \lambda\|\nabla\vec{u}\|^2_{L^2(\Omega)} + \|T(\vec{x}-\vec{u}) - S(\vec{x})\|^2_{L^2(\Omega)}, \quad (2)$$

where λ is a positive number indicating the weight of regularity. SSD model (2) has been widely used in practice because of its efficiency and simplicity. However, it is very sensitive to image noise and the weight parameter λ: small λ results an unstable and discontinuous deformation field, meanwhile large λ leads to inaccurate result, and may yield a nonphysical deformation field due to unreasonable restrictions[7].

Maximum likelihood estimate (MLE), or equivalently minimum negative log-likelihood estimate, as an improvement and generalization of SSD model, eliminates these problems by considering the points in the residue image as independent and identically distributed random variables with zero mean and unknown variance σ. In this paper we demonstrate our theory and compare the results using Gauss distribution, but one can assume Laplace or other types of distributions as well, according to particular applications. In this case, the joint distribution of the residue is presented as

$$P\left(\{T(\vec{x}-\vec{u}) - S(\vec{x}) | x \in \Omega\}\right) = \prod_{x\in\Omega} G_\sigma(T(\vec{x}-\vec{u}) - S(\vec{x}))$$

in discrete case, where $G_\sigma(z) = \exp(-z^2/2\sigma^2)/\sqrt{2\pi}\sigma$. So the negative log-likelihood is approximately

$$\int_\Omega \frac{|T(\vec{x}-\vec{u}) - S(\vec{x})|^2}{2\sigma^2} d\vec{x} + \frac{|\Omega|}{2}\log 2\pi\sigma^2 \quad (3)$$

in continuous case, where $|\Omega|$ is the volume of Ω. Combining the penalty term and (3), we now produce the energy functional of the so-called global Gaussian model (Gaussian for

short) as follows:

$$E[\vec{u},\sigma] = \lambda\|\nabla\vec{u}\|^2_{L^2(\Omega)} + \frac{1}{2\sigma^2}\|T(\vec{x}-\vec{u}) - S(\vec{x})\|^2_{L^2(\Omega)} + \frac{|\Omega|}{2}\log 2\pi\sigma^2, \tag{4}$$

where λ is again the regularity weight. The first variation of σ gives

$$\sigma^2 = \frac{1}{|\Omega|}\int_\Omega |T(\vec{x}-\vec{u}) - S(\vec{x})|^2 d\vec{x}$$

and the evolution of the E-L equation of u associated with $E[\vec{u},\sigma]$ is

$$\begin{cases} \dfrac{\partial\vec{u}}{\partial t} = \lambda\Delta\vec{u} + \dfrac{1}{\sigma^2}\left(T(\vec{x}-\vec{u}) - S(\vec{x})\right)\nabla T|_{\vec{x}-\vec{u}} \quad \text{in } \Omega, \\ \left.\dfrac{\partial\vec{u}}{\partial\vec{n}}\right|_{\partial\Omega} = 0 \end{cases} \tag{5}$$

where $\vec{n}$ is the outer normal of boundary $\partial\Omega$. This model does not require $T(\vec{x}-\vec{u})$ and $S(\vec{x})$ to be pointwise close as in SSD. It allows certain variability and hence is more robust in matching images with noises.

Gaussian (4) proves its power in registration where the variance throughout the images is homogeneous, but shows low efficiency and accuracy in matching small objects of low contrast: the residue $T(\vec{x}-\vec{u})-S(\vec{x})$ and gradient ∇T at these objects are much smaller than those at large objects with high contrasts, so they contribute little to the deformation velocity as the second term on the right side in (5). The consequence is that these small objects cannot be matched accurately. That is our motivation of partitioning the domain into several regions according to different residue variances, and optimize the variance on each region to improve efficiency and accuracy of the deformation.

In next section we present our model as a minimization problem of a level set formulated energy functional that combines penalty terms and negative log-likelihood of the residue in each region. In Section 3 we provides our numerical algorithm and experimental results using synthetic and real data.

2. PROPOSED MODEL

To demonstrate our idea in a simple way, we assume only two levels of variances in the residue image. Let C be the curve that partitions the domain Ω into two regions where the residue has different variances σ_1 and σ_2. By introducing the level set function ϕ such that $C = \{\vec{x} : \phi(\vec{x}) = 0\}$, we present one region as $\{\vec{x} : \phi(\vec{x}) > 0\}$ and another as $\{\vec{x} : \phi(\vec{x}) < 0\}$[8]. Now the partition can be obtained automatically by the evolution of ϕ. Combining negative log-likelihood in each region as in (4), and the regularity of $\vec{u}$ and C, our level set formulated energy functional becomes

$$\begin{aligned} & E[\vec{u},\phi,\sigma_1,\sigma_2] \\ =\ & \frac{\lambda}{2}\int_\Omega |\nabla\vec{u}|^2 d\vec{x} + \mu\int_\Omega |\nabla H(\phi)| \\ & + \frac{1}{2}\int_\Omega H(\phi)\left(\frac{1}{\sigma_1^2}|T(\vec{x}-\vec{u}) - S(\vec{x})|^2 + \log\sigma_1^2\right) \\ & + \frac{1}{2}\int_\Omega (1-H(\phi))\left(\frac{1}{\sigma_2^2}|T(\vec{x}-\vec{u}) - S(\vec{x})|^2 + \log\sigma_2^2\right). \end{aligned} \tag{6}$$

where λ and μ are positive numbers standing for weights of the smoothness of $\vec{u}$ and length of C, as the first two integrals in (6). $H(\cdot)$ is the Heaviside function: $H(\phi)$ and $1-H(\phi)$ are indicator functions of the two regions where the residue has variance σ_1 and σ_2, respectively. The latter two integrals in (6) are the negative log-likelihood in those two regions. We solve the energy minimization problem via calculus of variation: the first variations of σ_1 and σ_2 provide

$$\sigma_1^2 = \frac{\int_\Omega H(\phi)(T(\vec{x}-\vec{u}) - S(\vec{x}))^2 d\vec{x}}{\int_\Omega H(\phi) d\vec{x}} \tag{7}$$

and

$$\sigma_2^2 = \frac{\int_\Omega (1-H(\phi))(T(\vec{x}-\vec{u}) - S(\vec{x}))^2 d\vec{x}}{\int_\Omega (1-H(\phi)) d\vec{x}}, \tag{8}$$

the evolution of the E-L equation of ϕ associated with (6) is

$$\begin{cases} \dfrac{\partial\phi}{\partial t} = \delta(\phi)\left\{\mu\,\mathrm{div}\dfrac{\nabla\phi}{|\nabla\phi|} \right. \\ \left. -\dfrac{1}{2}\left[\left(\dfrac{1}{\sigma_1^2} - \dfrac{1}{\sigma_2^2}\right)|T(\vec{x}-\vec{u}) - S(\vec{x})|^2 + \log\dfrac{\sigma_1^2}{\sigma_2^2}\right]\right\} \\ \quad \text{in } \Omega, \\ \left.\dfrac{\delta(\phi)}{|\nabla\phi|}\dfrac{\partial\phi}{\partial\vec{n}}\right|_{\partial\Omega} = 0 \end{cases} \tag{9}$$

and the evolution of $\vec{u}$ is

$$\begin{cases} \dfrac{\partial\vec{u}}{\partial t} = \lambda\Delta\vec{u} + \\ \left(\dfrac{H(\phi)}{\sigma_1^2} + \dfrac{1-H(\phi)}{\sigma_2^2}\right)(T(\vec{x}-\vec{u}) - S(\vec{x}))\nabla T|_{\vec{x}-\vec{u}} \\ \quad \text{in } \Omega, \\ \left.\dfrac{\partial\vec{u}}{\partial\vec{n}}\right|_{\partial\Omega} = 0 \end{cases} \tag{10}$$

where $\vec{n}$ is the outer normal of boundary $\partial\Omega$, and δ is the derivative of H, i.e. Dirac function. Now we are ready to discretize equations (7)-(10) and solve them using computer.

3. NUMERICAL EXPERIMENTS

In our implementation, we use $C^\infty(\bar{\Omega})$ regularization H_ϵ of the Heaviside function $H_\epsilon(z) = \frac{1}{2}\left(1 + \frac{2}{\pi}\arctan\left(\frac{z}{\epsilon}\right)\right)$

and its derivative $\delta_\epsilon(z) = \frac{1}{\pi}\frac{\epsilon}{\epsilon^2+z^2}$ [8]. The outline of our algorithm is as follows: we set $\vec{u}^0 = 0$ and ϕ^0 to be the signed distance function of any initial curve in Ω. In k-th iteration, we calculate $\sigma_1(\phi^k, \vec{u}^k)$ and $\sigma_2(\phi^k, \vec{u}^k)$ using (7) and (8), and solve ϕ^k and $\vec{u}^k$ from (9) and (10). We apply semi-implicit scheme and use AOS algorithm to speed up the computation[9].

Now we test our model using both artificial and clinical data. The first experiment takes a pair of 2D synthetic images of dimensions 120×120, T and S, shown in Fig.1(a)(b). Each of them consists a large object of intensity 1, a small object (in the square) of 0.05 and background of 0.04. The square areas in Fig.1(a)(b) are enlarged and shown in the upper row of Fig.1(g). We apply Gaussian (4) and proposed model (6) to align this pair of images using the same time step $dt = 0.01$ and compare the results. Fig.1(c)(d) shows the deformed regular grid using the deformations $\vec{u}$ obtained by model (4) and (6). It is evident that the small object is deformed using proposed model, but there is no deformation observed using Gaussian. The reason is that the variance σ is 0.015 after 250 iterations by Gaussian in, which is even greater than the initial residue 0.01(=0.05-0.04) on small objects. At the same time, proposed model (6) provides a partition curve as shown in Fig.1(h): variance inside the curve is $\sigma_1 = 5 \times 10^{-3}$ and outside is $\sigma_2 = 6 \times 10^{-6}$, which is much smaller than initial residue 0.01, hence deformation on small objects occurred. The difference between the local deformations obtained by these two models are significant, as shown in the lower row of Fig.1(g). From Fig.1(e)(f) we can see the total and local (in the square) correlations obtained by proposed model (dashed lines) increase much faster than Gaussian (solid lines) in the first 300 iterations. Notice that local correlation by proposed model significantly increased after few iterations and reached 0.84 after 300 iterations, but the one by Gaussian barely changed (always less than 0.72) during the same time. This experiment shows the efficiency and accuracy of proposed model (6).

The second experiment tests proposed model using chest MR images T and S, shown in Fig.2(a)(b). The square areas in Fig.2(a)(b) consist the spinal core, which has much lower contrasts than soft tissues and is hard to match using Gaussian, although it is of great importance in modern radiation therapy. From our experimental results we can see an overall improvement of accuracy using proposed model, comparing the residue obtained by model (4) and (6), as shown in Fig.2(d)(e). Again the total correlation obtained by proposed model (dashed line) increases faster than Gaussian (solid line), and reached higher than 0.97, while Gaussian is lower than 0.96, after 200 iterations, as shown in Fig.2(f). The improvement of efficiency and accuracy in matching spinal cores can also be seen from the local (in the square) correlations by two models, as shown in Fig.2(g). S and deformed T by model (4) and (6) in the square are shown in Fig.2(h)(i)(j). In the same area, the initial residue, and the residues obtained

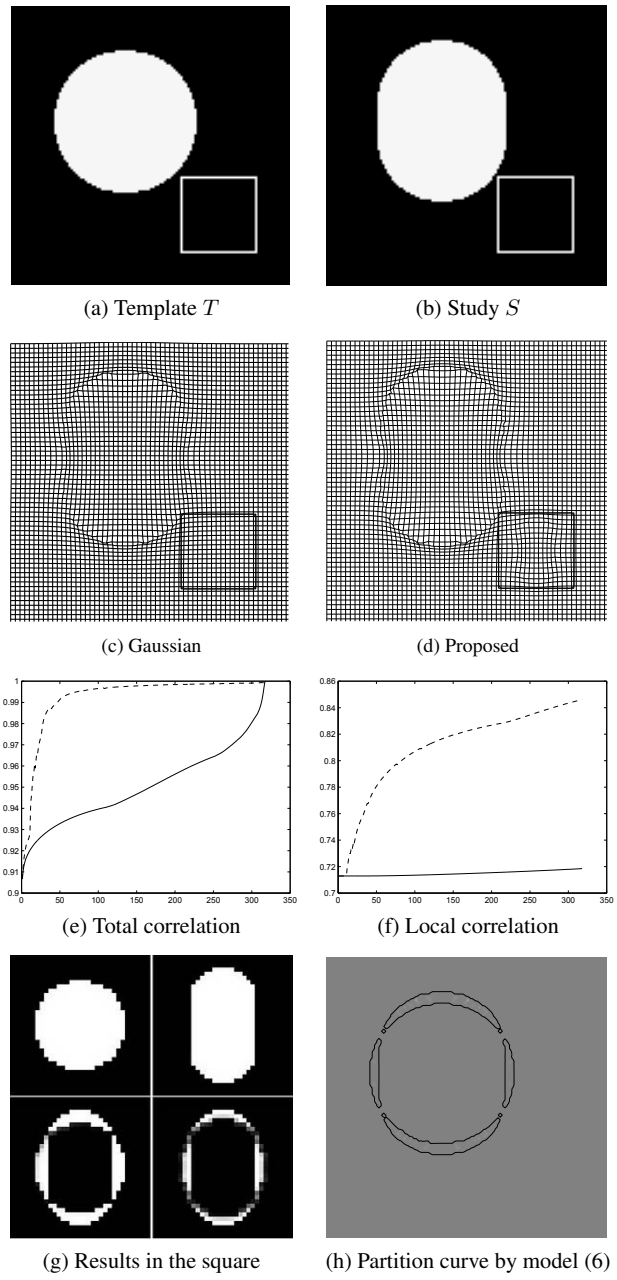

(a) Template T (b) Study S

(c) Gaussian (d) Proposed

(e) Total correlation (f) Local correlation

(g) Results in the square (h) Partition curve by model (6)

Fig. 1. Example on synthetic images. (a)(b) are given images T and S. (c)(d) are the deformation fields obtained by model (4) and (6) respectively. Deformation can be observed in the square using proposed model, as shown in (d), but not by Gaussian as in (c). (e) illustrates the total correlations obtained by Gaussian (solid line) and proposed model (dashed line) respectively. (f) indicates the local correlations restricted in the square as shown in (a)(b) using Gaussian (solid line) and proposed model (dashed line). Two images in the upper row of (g) are the enlarged squares in (a)(b) respectively. Two images in the lower row of (g) are the residue in the square after deformation using Gaussian and proposed model respectively. (h) shows the partition curve obtained by proposed model after 250 iterations.

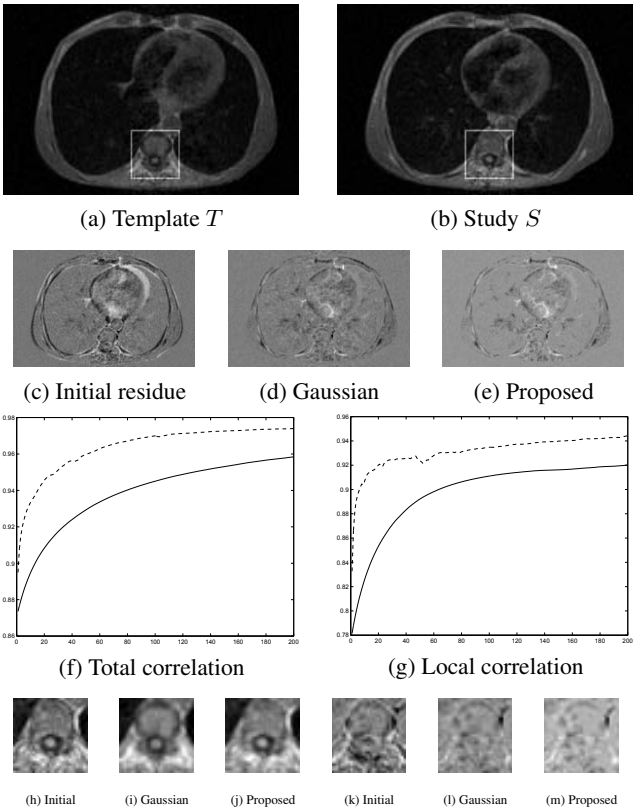

(a) Template T (b) Study S

(c) Initial residue (d) Gaussian (e) Proposed

(f) Total correlation (g) Local correlation

(h) Initial (i) Gaussian (j) Proposed (k) Initial (l) Gaussian (m) Proposed

Fig. 2. Example on chest MR images. (a)(b) are two given images T and S. (c) is the initial residue $T(\vec{x}) - S(\vec{x})$. (d)(e) are the residues $T(\vec{x} - \vec{u}) - S(\vec{x})$ after deformations using Gaussian and proposed model. (f)(g) are the total and local (in the square) correlations obtained by Gaussian (solid line) and the proposed model (dashed line) respectively. (h) is the enlarged square in (b). (i)(j) are deformed T, i.e.$T(\vec{x} - \vec{u})$, in the square obtained by Gaussian and proposed model. (k) is the initial residue in the square in (a)(b). (l)(m) are the local residue $T(\vec{x} - \vec{u}) - S(\vec{x})$ by Gaussian and proposed model respectively.

by model (4) and (6) are shown by Fig.2(k)(l)(m), from which the improvement of accuracy by proposed model can be observed. This experiment demonstrates the improvement of proposed model (6), and proves its ascendency in registration in radiation therapy where fine structures of low contrasts need to be matched as well.

4. CONCLUSION

This paper provides a general framework in deformable registration where the matching is allowed to vary in different regions of the domain. The partition of the domain is obtained by optimizing the fitting of the residue image to certain distribution with zero mean and different variances. We proposed our model as a minimization problem of an energy functional that combines the negative log-likelihood of the residue image in each region, smoothness of the deformation field and length of the partition curve. By taking different variances in each region, the deformation becomes more efficient and accurate, which is shown by the experimental results on synthetic and clinical data.

5. REFERENCES

[1] G.H. Olivera, K. Ruchala, W. Lu, J. Kapatoes, P. Reckwerdt, R. Jeraj, , and R. Mackie, "Evaluation of patient setup and plan optimization strategies based on deformable dose registration," *Int. J. Radiat. Oncol. Biol. Phys.*, vol. 53, pp. S188–9, 2003.

[2] W. Lu, M. Chen, G. Olivera, K. Ruchala, and T. Mackie, "Fast free-form deformable registration via calculus of variations," *Physics in Medicine and Biology*, vol. 49, pp. 3067–3087, 2004.

[3] M.M. Coselmon, J.M. Balter, D.L. McShan, and M.L. Kessler, "Mutual information based ct registration of the lung at exhale and inhale breathing states using thin-plate splines," *Med. Phys.*, vol. 31, pp. 2942–8, 2004.

[4] H. Wang, L. Dong, J. O'Daniel, R. Mohan, A. Garden, K. Ang, D. Kuban, M. Bonnen, J. Chang, and R. Cheung, "Validation of an accelerated 'demons' algorithm for deformable image registration in radiation therapy," *Phys. Med. Biol.*, vol. 50(12), pp. 2887–2905, 2005.

[5] E. Schreibmann and L. Xing, "Narrow band deformable registration of prostate magnetic resonance imaging, magnetic resonance spectroscopic imaging, and computed tomography studies," *Int. J. Radiat. Oncol. Biol. Phys.*, vol. 62, pp. 595–605, 2005.

[6] W. Lu, G.H. Olivera, Q. Chen, M. Chen, and K. Ruchala, "Automatic re-contouring in 4d radiotherapy," *Physics in Medicine and Biology*, vol. 51, pp. 1077–1099, 2006.

[7] D. Hill, P. Batchelor, M. Holden, and D. Hawkes, "Topical review: medical image registration," *Physics in Medicine and Biology*, vol. 46, pp. 1–45, 2001.

[8] T.F. Chan. and L.A. Vese, "Active contour without edges," *IEEE Trans. on Img. Proc.*, vol. 10(2), pp. 266–277, 2001.

[9] J. Weickert, B. Romeny, and M. Viergever, "Efficient and reliable schemes for nonlinear diffusion filtering," *IEEE Trans. on Img. Proc.*, vol. 7(3), pp. 398–410, 1998.